



HAL
open science

Comparing strategies for improving efficiencies in vacuum processed Cu₂ZnSnSe₄ solar cells

Louis Grenet, Abdul Aziz Suzon, Fabrice Emieux, Frédéric Roux

► To cite this version:

Louis Grenet, Abdul Aziz Suzon, Fabrice Emieux, Frédéric Roux. Comparing strategies for improving efficiencies in vacuum processed Cu₂ZnSnSe₄ solar cells. *Journal of Renewable and Sustainable Energy*, 2018, 10, pp.043503. 10.1063/1.5034526 . cea-02474077

HAL Id: cea-02474077

<https://cea.hal.science/cea-02474077>

Submitted on 11 Feb 2020

HAL is a multi-disciplinary open access archive for the deposit and dissemination of scientific research documents, whether they are published or not. The documents may come from teaching and research institutions in France or abroad, or from public or private research centers.

L'archive ouverte pluridisciplinaire **HAL**, est destinée au dépôt et à la diffusion de documents scientifiques de niveau recherche, publiés ou non, émanant des établissements d'enseignement et de recherche français ou étrangers, des laboratoires publics ou privés.

Comparing strategies for improving efficiencies in vacuum processed $\text{Cu}_2\text{ZnSnSe}_4$ solar cells

Louis Grenet, Md Abdul Aziz Suzon, Fabrice Emieux, and Frédéric Roux

Citation: [Journal of Renewable and Sustainable Energy](#) **10**, 043503 (2018); doi: 10.1063/1.5034526

View online: <https://doi.org/10.1063/1.5034526>

View Table of Contents: <http://aip.scitation.org/toc/rse/10/4>

Published by the [American Institute of Physics](#)

Articles you may be interested in

[Numerical investigations of the effect of rotating and non-rotating shaft on aerodynamic performance of small scale urban vertical axis wind turbines](#)

[Journal of Renewable and Sustainable Energy](#) **10**, 043302 (2018); 10.1063/1.5025078

[Hybrid dye-sensitized solar cells with graphene—A convenient method to seal liquid state devices](#)

[Journal of Renewable and Sustainable Energy](#) **10**, 043504 (2018); 10.1063/1.5037150

[Oxygen aging time: A dominant step for spiro-OMeTAD in perovskite solar cells](#)

[Journal of Renewable and Sustainable Energy](#) **10**, 043702 (2018); 10.1063/1.5031167

[Effect of \$\text{Cu}_2\text{O}\$ hole transport layer and improved minority carrier life time on the efficiency enhancement of \$\text{Cu}_2\text{NiSnS}_4\$ based experimental solar cell](#)

[Journal of Renewable and Sustainable Energy](#) **10**, 043502 (2018); 10.1063/1.5037471

[Mid-wavelength high operating temperature barrier infrared detector and focal plane array](#)

[Applied Physics Letters](#) **113**, 021101 (2018); 10.1063/1.5033338

[A new representation model of standard and available active materials for electrochemical batteries](#)

[Journal of Renewable and Sustainable Energy](#) **10**, 044101 (2018); 10.1063/1.5029276

Comparing strategies for improving efficiencies in vacuum processed $\text{Cu}_2\text{ZnSnSe}_4$ solar cells

Louis Grenet,^{1,2,a)} Md Abdul Aziz Suzon,^{1,2} Fabrice Emieux,^{1,2}
and Frédéric Roux^{1,2}

¹Univ. Grenoble Alpes, F-38000 Grenoble, France

²CEA, LITEN, 17, rue des Martyrs, F-38054 Cédex 09 Grenoble, France

(Received 12 April 2018; accepted 25 June 2018; published online 11 July 2018)

In this study, we detail a $\text{Cu}_2\text{ZnSnSe}_4$ based solar cell fabrication process based on the selenization of metallic precursor stacks with elemental Se. 9.4% efficient devices without antireflection coating have been obtained. First, reproducibility issues of the process are carefully shown and discussed. It is demonstrated that device performances are strongly impacted by the precise control of the precursor composition. Then, starting from this robust process, a review of existing strategies to improve kesterite efficiencies is conducted. A significant increase in efficiency (+1.4% absolute efficiency and +50 mV V_{OC}) is obtained with absorber surface treatment and post-annealing, while no effect of Ge incorporation in the precursor stack is observed. This contradictory result to most of the recent publications raises the question of the universality of this strategy to improve kesterite solar cell performance. Finding a universal activation step to boost kesterite efficiencies and bring it to the market remains a crucial need for the community. *Published by AIP Publishing.* <https://doi.org/10.1063/1.5034526>

I. INTRODUCTION

In the past decade, the $\text{Cu}_2\text{ZnSn}(\text{S},\text{Se})_4$ (CZTSSe) absorber has attracted a lot of attention in the thin film photovoltaic (PV) community because of its potential to replace the $\text{Cu}(\text{In},\text{Ga})(\text{S},\text{Se})_2$ absorber in thin film solar cell technology without using critical raw materials. However, despite similar electro-optical properties,¹ the maximum certified efficiency for CZTSSe solar cells is limited to 12.6%,² which is far from 22.9% achieved by chalcopyrite devices.³ The large deficit in open circuit voltage (the V_{OC} deficit is expressed as $E_{\text{G}}/q - V_{\text{OC}}$, where E_{G} is the absorber bandgap and q the elemental charge) in kesterite solar cells is mainly evoked to explain these lower performances,^{4,5} and many routes have been tested by the kesterite community to solve this issue. Among the solutions proposed in the literature to decrease the V_{OC} deficit and improve performances in CZTSSe solar cells made by vacuum techniques, one can find the following: increasing the alkali (Na) doping in the absorber with the introduction of a Mo:Na back electrode,⁶ adding a Se capping on top of the metallic precursors,⁷ introducing a Ge nanolayer in the precursor stacks,⁸ or improving the absorber surface by chemical etching.^{9,10} All these strategies lead to substantial improvements of the related baseline processes with an absolute efficiency increase in the 1%–3% range. However, the absence of the standard reference device in the kesterite community and the number of possible routes to synthesize absorber layers¹¹ can be a drag on the discovery of a universal solution to improve solar cell performances. Thus, it is of prime importance to discriminate between solutions which improve particular processes to those which can be beneficial for the CZTSSe material regardless of its synthesis route.

In this study, we propose to test different already published strategies to boost the CZTSSe efficiency in order to give a tentative view of their universality and their possible transposition

^{a)} Author to whom correspondence should be addressed: louis.grenet@cea.fr

to slightly different baseline processes. To this purpose, a very precise description of our reference CZTSe solar cell fabrication process with particular attention paid to the reproducibility issues is first given before the implementation of the aforementioned strategies to improve efficiencies of our devices. The PV properties of samples from the baseline process and from alternative routes are compared to assess the impact of these strategies.

In previous works, we described a CZTSSe synthesis process based on the selenization of ZnS/Cu/Sn stacks of precursors deposited by radio-frequency sputtering and e-beam evaporation, leading to devices with power conversion efficiencies of 6.0%¹² and 7.0%.¹³ Despite these promising results, precursor stacks have been recently replaced by pure metallic (Cu, Zn, and Sn) stacks fully deposited by direct-current sputtering in order to make the process more compatible with industrialization (deposition time and homogeneity). The change in precursor stacks imposed to totally redefine the Mo back electrode (the previous Mo layer was totally selenized with this new process) and the annealing step. This new process is detailed thereafter.

II. EXPERIMENTAL

A. Sample preparation

CZTSe-based solar cells are fabricated on Soda-Lime Glass (SLG) automatically cleaned and dried in a Pluritank USC120 MK4 from Novatec with successive ultrasonic and soap baths. A Mo tri-layered back contact is deposited by DC-sputtering in an Alliance Concept Cluster Line equipment: a first 500 nm layer is sputtered at 0.4 Pa and 2 W cm^{-2} to ensure electrical conductivity, a 200 nm low density layer is then deposited at 1 Pa and 0.5 W cm^{-2} to limit the MoSe₂ formation, while a 20 nm sacrificial layer is sputtered at 0.1 Pa and 2 W cm^{-2} to improve the CZTSe/Mo electrical contact. A 500 nm Mo:Na layer can be deposited at 0.4 Pa and 2 W cm^{-2} below the Mo-trilayer to increase the Na content in the absorber due to Na diffusion during the annealing process.

Cu ($5 \text{ nm} \pm 2 \text{ nm}$)/Sn ($245 \text{ nm} \pm 20 \text{ nm}$)/Cu ($190 \text{ nm} \pm 10 \text{ nm}$)/Zn ($160 \text{ nm} \pm 10 \text{ nm}$) metallic precursors are deposited by direct current sputtering in a Perkin Elmer deposition chamber at 0.13 Pa and 1.3 W cm^{-2} without intentionally heating the substrate. A 300 nm Se layer capping is thermally evaporated on top of the metallic precursors in a SVTA (SVT Associates, Inc.) deposition chamber at 1.3×10^{-4} Pa and without substrate heating. Ge can optionally be introduced before and after precursor sputtering by e-beam evaporation in a Univex deposition chamber at 1×10^{-3} Pa and without substrate heating. Precursor batches of 24 samples are processed simultaneously. Variability in the precursor thicknesses corresponds to the minimum and maximum values measured on individual reference layers (Cu, Zn, and Sn) deposited on glass.

$2.5 \times 2.5 \text{ cm}^2$ samples are annealed in a tubular lamp furnace in an Ar atmosphere. Samples are placed in a 21 cm^3 graphite susceptor along with 2 Se pellets ($m_{\text{Se}} = 48 \pm 8 \text{ mg}$). The annealing profile consists in a first step at 320 °C and 100 Pa during 20 min followed by a 5 min step at 520 °C and 8.5×10^4 Pa. Heating ramps are fixed at 1 °C s^{-1} , while natural cooling allows us to decrease from 520 °C to 100 °C in 20 min.

An optional absorber surface etching can be used before buffer layer deposition. Different etching solutions have been tested: a hot hydrochloric solution, a potassium permanganate solution, a sulfur ammonium solution, and different combinations of these solutions. The hot hydrochloric bath consists of a 10% HCl solution heated at 60 °C on a hot plate in which samples are immersed for 10 min. The potassium permanganate bath is a KMnO₄/H₂SO₄ solution prepared from the dissolution of 39.5 mg of solid KMnO₄ in 48.6 ml of deionized water and 1.4 ml of 95% H₂SO₄. Samples are dipped for 40 s into the bath at room temperature. The (NH₄)₂S bath is made from a commercially available 50% solution diluted at 25%. Samples are immersed in (NH₄)₂S for 2 min at room temperature.

A 70 nm CdS buffer layer is deposited by chemical bath deposition in a double wall beaker heated at 80 °C. Cadmium acetate (1 mM), thiourea (5.1 mM), ammonium acetate (20 mM), and ammonia (0.3 mM) are stirred at 600 rpm, and samples are immersed in the solution for 15 min. Eight samples can be processed simultaneously. A 50 nm/250 nm i-ZnO/ZnO:Al (Al₂O₃ 2 at. %) window layer is RF-sputtered in a MRC2 chamber without intentional sample heating and with

a 1% and 0.05% Ar:O₂ reactive gas, respectively. The typical sheet resistance of the window layer is $25 \Omega \square^{-1}$. Ni (50 nm)/Al (500 nm) grids (1 mm diameter circle, 3% shading) are thermally evaporated on top of the solar cell. The Mo back contact is open by manually removing the CZTSe/CdS/ZnO stack and improved with an indium coating put with an iron soldering. $0.5 \times 0.5 \text{ cm}^2$ solar cells are isolated with an automated mechanical scribe. No anti-reflecting coating is used on these samples.

B. Characterization

The composition of the absorbers is determined by X-Ray Fluorescence (XRF) in a FISCHERSCOPE[®] X-RAY XDV-SDD equipment working at 50 kV. A Spectra-Nova's CT Series Solar Cell Tester is used to perform current-voltage (J-V) measurements under the simulated AM1.5G spectrum (100 mW cm^{-2}). All J-V measurements (light and dark) are performed at 25 °C in a four-point probe configuration. External quantum efficiency (EQE) measurements are carried out using ReRa Spequest.

III. RESULTS AND DISCUSSION

A. Baseline process and alternative routes

In the baseline process, CZTSe absorber layers are synthesized by annealing Mo/Cu/Sn/Cu/Zn/Se (Mo/Prec/Se) stacks in a Se atmosphere with the conditions described in Sec. II, resulting in a Mo/MoSe₂ (~500 nm)/CZTSe (~1500 nm) structure. Raman spectroscopy with 532 nm excitation and X-Ray diffraction have been used (not shown) to prove the existence of a kesterite phase but are not systematically employed since they are insufficient to exclude the presence of secondary phases.¹⁴ On the contrary, the composition of the samples is systematically measured with XRF after absorber synthesis in 9 points per sample. The cationic composition is estimated from this measurement with an uncertainty linked to the measurement procedure rather than an inhomogeneity in the sample since 9 measurements at the same point reveal a similar variability.

In the present study, samples from two batches of precursors are presented (batch 1 and batch 2). The first samples of each batch (1A, 1B, 1C, and 1D for batch 1 and 2A and 2B for batch 2) are made with the standard procedure, while alternative routes to improve the process are compared (samples 1E, 1F, 1G, 1H, and 2C). The list of the samples and their cationic composition is given in Table I.

First, the influence of Se capping has been tested (sample 1E: Mo/Prec). The improvement of kesterite devices with introduction of an ultrathin Ge layer (5 nm below and above the Cu/Sn/Cu/Zn precursor stack) has been tested in the first stack of precursors without a Se capping

TABLE I. List and composition (XRF measurements) of the CZTSe samples presented in the first part of the study.

#	Stack	Cationic composition (XRF)			Atomic ratio		
		Cu (at. %)	Zn (at. %)	Sn (at. %)	Cu/(Sn + Zn)	Zn/Sn	Cu/Sn
1A	Mo/Prec/Se	42.7 ± 0.6	29.1 ± 0.3	28.0 ± 0.8	0.74	1.05	1.52
1B	Mo/Prec/Se	42.9 ± 0.4	29.1 ± 0.4	28.0 ± 0.8	0.75	1.04	1.53
1C	Mo/Prec/Se	43.1 ± 0.5	28.8 ± 0.7	28.1 ± 1.1	0.76	1.03	1.48
1D	Mo/Prec/Se	43.0 ± 0.8	29.5 ± 0.6	27.5 ± 1.3	0.75	1.08	1.57
1E	Mo/Prec	42.9 ± 0.5	28.9 ± 0.4	28.2 ± 0.9	0.75	1.03	1.52
1F	Mo/Ge5/Prec/Ge5	43.0 ± 0.7	28.9 ± 0.4	28.1 ± 1.0	0.75	1.03	1.53
1G	Mo/Ge5/Prec/Ge5/Se	42.9 ± 0.6	29.8 ± 0.4	27.4 ± 0.5	0.75	1.09	1.57
1H	MoNa/Mo/Prec/Se	42.9 ± 1.0	30.0 ± 0.9	27.1 ± 1.9	0.75	1.11	1.59
2A	Mo/Prec/Se	42.6 ± 0.7	29.4 ± 0.4	28.0 ± 0.9	0.75	1.05	1.53
2B	Mo/Prec/Se	42.6 ± 0.7	29.2 ± 0.5	28.2 ± 1.1	0.74	1.04	1.51
2C	Mo/Ge10/Prec/Ge10/Se	43.1 ± 0.6	29.0 ± 0.6	27.9 ± 1.1	0.76	1.04	1.55

(sample 1F: Mo/Ge5/Prec/Ge5) and with a Se capping (sample 1G: Mo/Ge5/Prec/Ge5/Se). Introduction of Ge has been tested also in the second stack of precursors with a 10 nm layer below and above the precursor stack (sample 2C: Mo/Ge10/Prec/Ge10/Se). A 500 nm Mo:Na layer has been introduced before the standard process to increase the Na content in the CZTSe absorber (sample 1H: MoNa/Mo/Prec/Se).

Photovoltaic properties [photovoltaic conversion efficiency (PCE), fill factor (FF), open circuit voltage (V_{OC}), and Short-circuit Current (J_{SC})] of the samples described in Table I are gathered in Fig. 1. For each sample, 16 solar cells have been fabricated, and the properties of all devices are represented by boxplots. Median values over the 16 cells obtained with the baseline process (batch 1) are $PCE = 7\% \pm 0.5\%$, $FF = 55\% \pm 3\%$, $V_{OC} = 396 \text{ mV} \pm 6 \text{ mV}$, and $J_{SC} = 31 \text{ mA cm}^{-2} \pm 1 \text{ mA cm}^{-2}$.

First, it is noticeable that the homogeneity (variability within one sample) and the reproducibility (variability from sample to sample) are not very good. Within one sample, the PCE variability up to 3% absolute in the worst case (1C) can be observed. This value is however equivalent or smaller than inhomogeneity obtained by similar vacuum processes.⁷ Unfortunately, this non-homogeneity issue is very rarely discussed in the literature since in most of the publications, only best performing devices are shown.

Reproducibility from sample to sample is also a crucial issue: even within a single batch of precursors, a 1% absolute efficiency variation in the median value over the 16 cells is observed between samples 1A and 1D. This variability is even larger when 2 batches are considered, and reference samples from batch 2 reveal significantly lower performances than those of batch 1, mainly due to a limited V_{OC} .

No clear evidence can explain the inhomogeneity (variability within one sample) issue in our samples. Different hypotheses have been drawn such as the localized presence of small inclusions (below the detection limit of our XRD or Raman setups) of minor phases at the surface or in the bulk (a clear correlation between a large amount of SnSe_2 and degradation of PV performances has been established in our samples; see [supplementary material](#)) or the small scale variation of the absorber composition, leading to a locally unfavorable composition. The

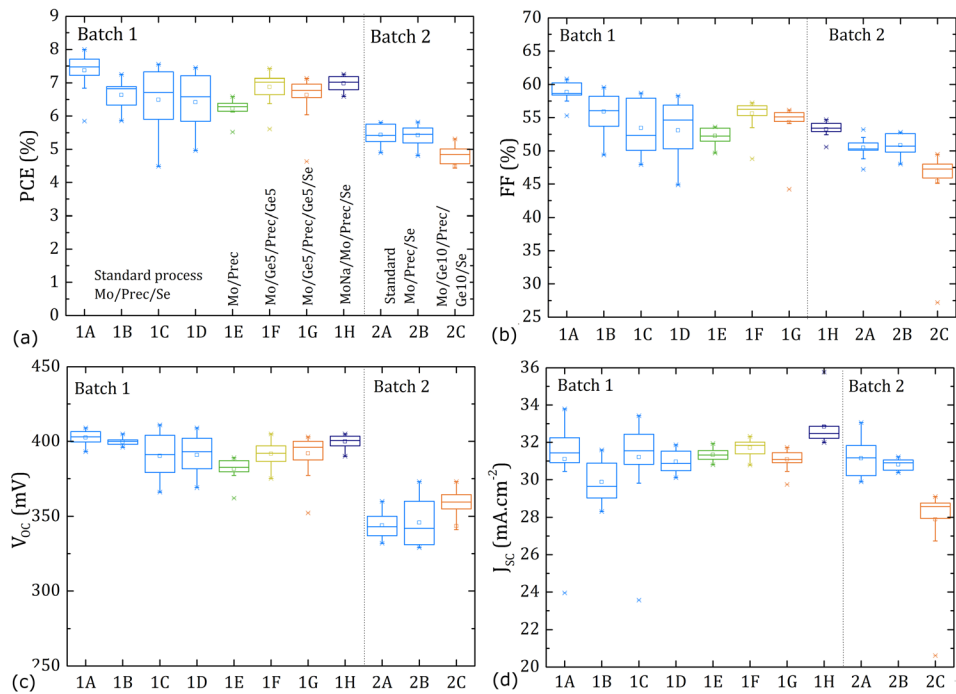


FIG. 1. Photovoltaic properties [(a) PCE, (b) FF, (c) V_{OC} , and (d) J_{SC}] of the samples described in Table I. In this representation, the median value is given by the horizontal line in the middle, while bottom and top parts of the box are related to the 25th and 75th percentiles, respectively.

degradation of performances due to the presence of pinholes in the layer has been excluded with systematic SEM top view analysis.

The reproducibility issue (sample to sample variation) has been attributed to the exact cationic composition of the precursors before the synthesis of the CZTSe absorber. Contribution of the annealing step to the performance variability cannot be totally excluded, but a systematic batch effect is observed: all samples from a single batch similarly processed always reveal closer performances than sample reproduction from batch to batch. This batch effect exists even when samples from different batches have been processed alternatively to test the non-controlled variations in the selenization furnace.

At first sight, this hypothesis seems to be contradicted by XRF results given in Table I since the composition of the samples from different batches is identical within the error bar of the measurements. However, it has been demonstrated in Ref. 15 that a significant variation of device performances can be obtained with a $\pm 0.5\%$ change in the cationic composition in the absorber. Additionally, due to species evaporation during the annealing process, precursor batches with different compositions can lead to absorbers with a more similar composition after annealing due to the self-regulation process.¹⁶ Measuring very accurately the composition of precursor stacks would be the key parameter to reduce the spreading in solar cell performances. Unfortunately, uncertainty on the measurements of the multi-layered metallic stacks with our XRF equipment is even worse than measuring homogeneous absorbers and does not allow us to discriminate the quality of different precursors. This difficulty in accurately controlling the sputtered precursor composition can probably explain the large variability in device performances observed in Ref. 17 and may be a trail to explain also that the best efficiencies demonstrated so far have been achieved by a liquid route for which the precursor composition control is easier.² Improving the reproducibility and homogeneity of kesterite devices simultaneously requires a methodology to locally and very precisely determine the composition of the absorber layer such as electron microprobe analysis¹⁸ in combination with large scale composition analysis such as XRF.

As a consequence, and due to the lower quality of the second batch of precursors, this study will mainly focus on the samples from batch 1. Within this batch (samples 1A to 1H), the different strategies to improve kesterite devices are compared with the reference process with particular attention paid to the variability obtained from sample 1A to sample 1D.

Contrary to our expectation and to the results published in the literature,^{6,8} no significant impact of the different strategies can be seen in Fig. 1. Particularly, PCE median values for samples 1F (introduction of Ge without Se capping), 1G (introduction of Ge with Se capping), and 1H (introduction of Mo:Na) are comprised between the values of samples 1A to 1D (baseline process). Some slight variations can however be noticed: the median efficiency for sample 1E (without Se capping and without Mo:Na nor Ge) is lower than in the other samples, mainly due to a lower median V_{OC} (-15 mV compared to the reference process). The PV properties of samples with Ge (1D and 1F) are very close to those of reference ones, while the introduction of Mo:Na in the back electrode slightly increases J_{SC} ($+1.5$ mA cm^{-2}) but does not obviously impact V_{OC} . However, all these variations are comparable with the process variability shown with samples 1A to 1D.

Thicker Ge nanolayers (10 nm) have been introduced as well below and above precursor stacks in a sample from batch 2 in order to ensure that the absence of the Ge effect in batch 1 is not linked to an insufficient Ge amount compared to Ref. 8. However, similar to results from batch 1, the introduction of a double 10 nm Ge layer does not improve PV performances of the device compared to the baseline process.

The absence of the Ge effect and to a lesser extent of the Mo:Na and Se capping effect seems to be contradictory to the results previously published in the literature. Small differences in the processes (thermal evaporation and not e-beam evaporation for Ge has been used in Ref. 8 for instance, maybe leading to a different Ge phase or to a different amount of GeO_2 deposited in the precursor stack) could be at the origin of different results. However, more fundamentally, it remains questionable whether device improvement with Ge is universal or results from a specific optimization of the process with Ge. The excellent results obtained in Ref. 8 with a

small addition of Ge can either be linked to a fundamental boosting effect of Ge or to a specific optimization of this specific process. In our case where the process has been optimized without Ge, the introduction of Ge does not play a beneficial role. An exactly similar question must be raised with other cationic substitutions (Ag for Cu¹⁹ and Mn for Zn,²⁰ for instance) which also show improved performances at a low substitution rate: is it a universal behavior or the result of a specific optimization process?

To date, the most efficient kesterite solar cell is based on a pure Cu₂ZnSn(S,Se)₄ absorber synthesized with a solution process allowing a very precise control of the sample composition.² Cationic substitution has not demonstrated yet the absolute improvement of kesterite devices, and a very accurate control of the precursor composition is a fundamental parameter to obtain very efficient and reproducible solar cells.

B. Surface etching and post-treatment annealing

Surface recombination is often cited in the literature as a culprit for limited efficiencies in kesterite devices.^{4,5} Different strategies have been tested to improve the CZTSSe surface prior to CdS deposition using a hot HCl solution (H),¹⁰ a KMnO₄/H₂SO₄ solution (K),⁹ or a (NH₄)₂S solution (S).⁹ The use of these solutions (H, K, and S) and the combination of different solutions (K + S and H + K + S) is presented thereafter on samples from the baseline process (Mo/Prec/Se) from batch 1 and compared with the most efficient sample of this batch (sample 1A).

The photovoltaic properties of the different samples are shown in Fig. 2 (open boxplots). The sample etched in hot hydrochloric acid (H) shows a similar behavior to the reference sample. On the contrary, the other treatments (K, S, K + S, and H + K + S) systematically and significantly (from 3% to 5% absolute PCE) degrade all PV properties of the device and particularly FF. The K solution seems to be the most detrimental treatment, but in the absence of reproducibility studies, it is impossible to draw definitive conclusions about the comparison between the different solutions.

Post-deposition annealing (PDA) is a frequently used technique to recover performances of degraded devices in thin film PV technology.²¹ As devices with an etch treatment have been

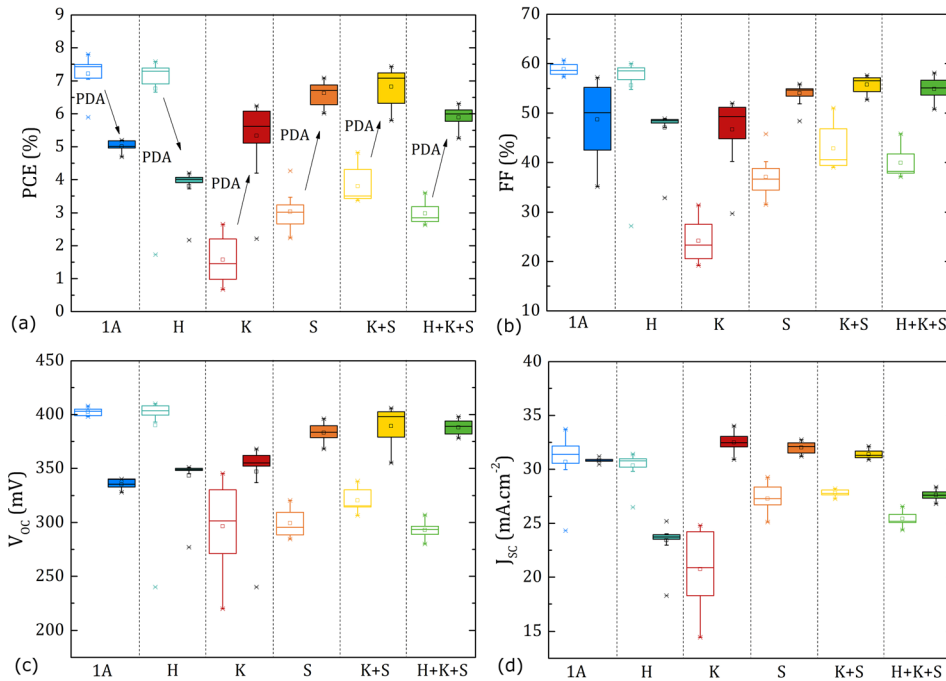


FIG. 2. PV properties [(a) PCE, (b) FF, (c) V_{OC}, and (d) J_{SC}] of the 16 solar cells defined on each sample with surface treatment (no etch and etch in H, K, S, K + S, and H + K + S solutions) before (open boxplots) and after (filled boxplots) post-annealing.

severely harmed compared to the reference solar cells, a PDA treatment of 200 °C for 10 min in air has been tested along with sample 1A for the sake of comparison. All cells have been placed on a hot plate in obscurity and measured again under the AM1.5G solar spectrum after a substantial light soaking treatment (at least 10 min under the solar spectrum before the measurement). The PV properties of the solar cells after PDA are depicted in Fig. 2 in filled boxplots.

Two very distinct behaviors are noticeable: sample 1A and H-treated sample performances are lower after PDA mainly due to a >50 mV V_{OC} loss, whereas all other etched samples recover roughly the 1A sample PV properties (without PDA). K- and H+K+S etched samples show slightly lower performances than the S- and K+S etched samples due to lower V_{OC} in the first case and lower J_{SC} in the second case.

Determining the exact role of each etching step on structural (composition modification and surface secondary phase suppression) and on PV (particularly the impact on interface recombination) properties is of prime importance to further improve the process and will be the subject of a future article.

PDA treatment has then been optimized in terms of annealing time and temperature to maximize device performances. This optimization has been conducted on two new S-etched samples from the precursor batch 2 with lower PCE than the reference batch 1 sample. The first sample has been successively annealed for 10 min on a hot plate in the dark at increasing temperature, while the second sample has been annealed in the dark at 210 °C for increasing time. The evolution of 3 solar cells (chosen for their different initial PV properties) for each sample during PDA optimization is depicted in Fig. 3. A substantial light soaking treatment (10 min under the AM1.5 spectrum) is systematically observed before the solar cell measurement.

On the first sample, no variation in PV properties occurs up to 100 °C. A significant increase in all PV properties is observable between 100 °C and 150 °C where a first maximum in FF is reached. After a small but significant minimum in FF around 180 °C, a new maximum is reached between 210 °C and 220 °C. All cells attain similar J_{SC} at this temperature (despite large discrepancy in initial J_{SC}) and keep the same value up to 180 °C where they start to

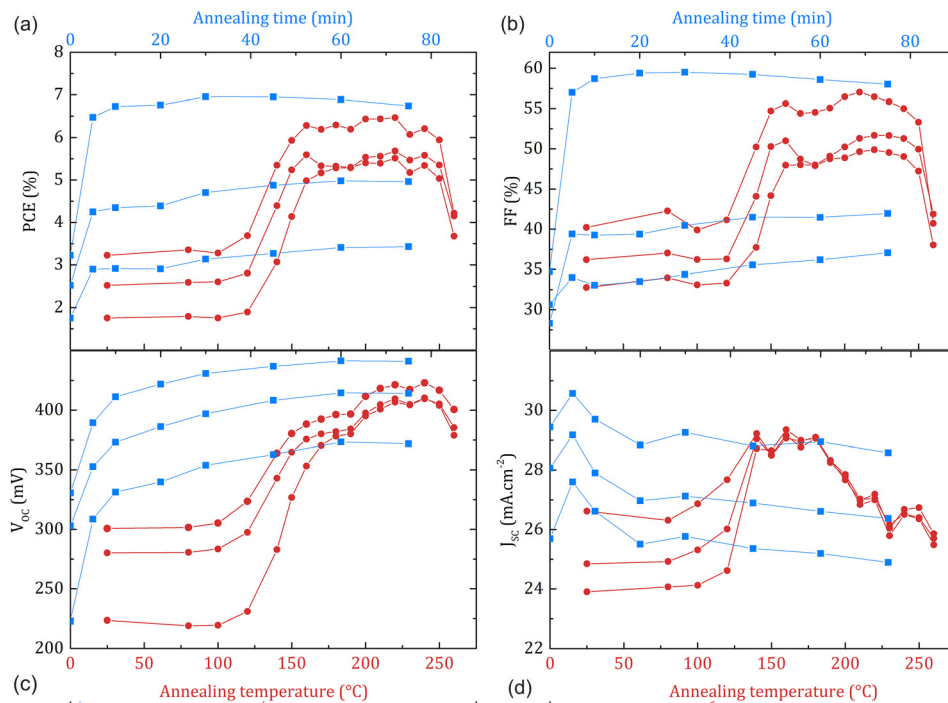


FIG. 3. Optimization of the PDA process. Red curves (bottom legend) show the PV properties [(a) PCE, (b) FF, (c) V_{OC} , and (d) J_{SC}] of the sample annealed at increasing temperature. Blue curves (top legend) show the PV properties [(a) PCE, (b) FF, (c) V_{OC} , and (d) J_{SC}] of the sample with cumulative annealing time. In each case, the evolution of three solar cells with different initial properties has been.

decrease. A first plateau is reached for V_{OC} in the 150 °C–180 °C range and then a second higher one in the 200 °C–240 °C range. Above 240 °C, FF and V_{OC} drop suddenly. The different evolution of V_{OC} , J_{SC} , and FF leads to a less clear evolution for PCE which is almost constant in the 150 °C–250 °C range of PDA. In order to maximize V_{OC} and FF, a PDA temperature of 210 °C has been selected.

PDA at 210 °C in the dark has then been tested for various times on the second sample. Annealing and measurements (including 10 min light soaking under AM1.5G) have been conducted successively, and the cumulative PDA time is depicted in Fig. 3 (blue curves). A huge increase in all PV properties is observed after the first 5 min PDA exposure, while different trends can be observed afterwards: the FF of the best cell increases up to 30 min before a slight decrease, whereas the FF of the worst cells increases up to 75 min. As far as V_{OC} is concerned, the longer the PDA, the better the V_{OC} . J_{SC} is improved by a 5 min PDA but starts to decrease again at longer annealing time. As a summary, a systematic improvement of PCE is observed for a 30 min PDA with most of the effect occurring in the first 5 min. A very slight decrease is then observed for the best cell, while cells with lower efficiencies continue to be improved by PDA up to 75 min. A 210 °C/60 min PDA has been chosen to maximize both PCE and V_{OC} of our solar cells.

C. Best devices

In this last part, the best solar cells fabricated with and without (the best cell from sample 1A) surface etching and PDA are compared. Both solar cells come from precursor batch 1 and consist of a Mo/Prec/Se stack annealed with the standard conditions. For the as-deposited cell (no etching nor PDA), the CdS buffer layer has been deposited directly after absorber synthesis, while for the second cell, a K + S etch of the surface has been made followed by a 210 °C/60 min PDA. It is worth noticing that in the first case, no significant evolution of the PV properties during exposure to AM1.5 is observed, while a long light soaking treatment (1 night under the AM1.5 spectrum) has been used before measuring the second cell. Dark and illuminated under AM1.5 spectrum J-V curves of these 2 best cells are depicted in Fig. 4(a), and the related EQE spectra are plotted in Fig. 4(b). PV properties extracted from the light, dark J-V curves and EQE spectra are summarized in Table II.

Both solar cells have very similar J-V curves with a J_{SC} value close to 33 mA cm⁻² and a comparable positive slope at J_{SC} (non-superposition of dark and light J-V curves) which has been attributed to the limited minority carrier collection length.²² The K + S + PDA sample reveals however a much better V_{OC} (457 mV, +50 mV) and consequently a better FF than the as-deposited cell. Due to this improved V_{OC} , a maximum PCE of 9.4% has been attained on the etched and annealed sample compared to a maximum 8.0% achieved with an as-deposited sample. These values have been obtained without using any antireflection coating. The diode saturation current (J_0), ideality factor (n), and series and shunt resistances (R_S and R_{Sh}) have

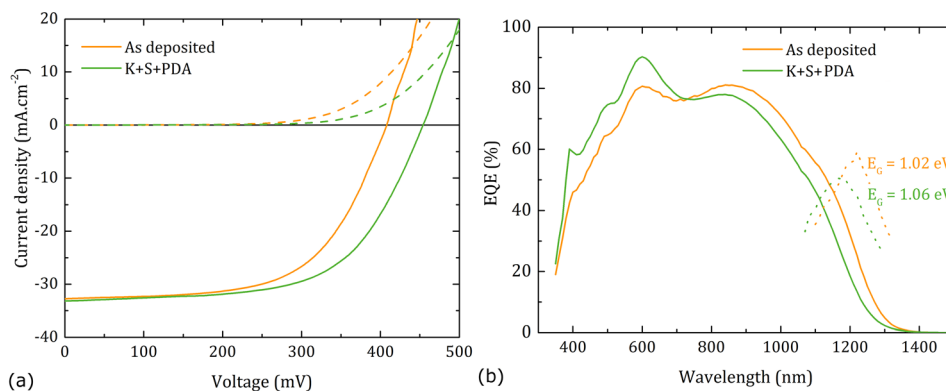


FIG. 4. (a) J-V characteristics of the best devices under the AM1.5G spectrum (continuous line) and in the dark (dashed line). (b) EQE spectra of the same solar cells. The 1st derivative of the EQE spectra to determine the absorber bandgap is plotted with dotted lines.

TABLE II. PV properties of the solar cells extracted from Figs. 4(a) and 4(b).

	Light				Dark				EQE	
	PCE (%)	FF (%)	V _{OC} (mV)	J _{SC} (mA cm ⁻²)	J ₀ (mA cm ⁻²)	n	R _S (Ω cm ²)	R _{Sh} (Ω cm ²)	E _G (eV)	V _{OC} deficit (mV)
As deposited	8.0	59.9	408	32.8	1.0x10 ⁻³	1.7	1.34	4038	1.02	610
K + S + PDA	9.4	62.0	457	33.2	2.4x10 ⁻⁴	1.6	1.45	3225	1.06	600

been extracted by fitting the dark J-V curves and are summarized in Table II. The main difference between both cells lies in a saturation current decreased by almost one order of magnitude for the K + S + PDA cell compared to the as-deposited one.

Comparing EQE spectra reveals however different behaviors between both cells. First, the EQE maximum is increased from 80% to 90% with the surface treatment, and EQE at short wavelengths is globally improved, which is attributed to the improvement of the window layer transmittance and the CdS crystallization due to the PDA. However, simultaneously, the long wavelength (>800 nm) response is lowered, and a shift in the absorber bandgap (estimated from the maximum of the first derivative of the EQE curve) is observed, leading to a similar J_{SC}. The increase in the bandgap from 1.02 eV to 1.06 eV is attributed to the Cu/Zn ordering in the absorber layer due to the PDA. Indeed, this relatively long annealing procedure at low temperature (210 °C for 60 min) is supposed to increase Cu/Zn ordering, and bandgap variations up to 0.1 eV can be caused by the different degrees of Cu/Zn disorder in Cu₂ZnSnSe₄ solar cells.²³ However, this higher bandgap can only account for 40 mV in the improved V_{OC}, and thus, a smaller V_{OC} deficit is obtained for the sample with the etched surface. Additionally, at constant performance, a 40 mV bandgap increase should be translated in a > 1.5 mA cm⁻² decrease in the J_{SC} value as well.²³ The latter effect is not observed (the maximum EQE is significantly increased), implying that both V_{OC} and J_{SC} are actually improved by the surface etching and PDA treatment.

IV. CONCLUSION

A precise description of the fabrication method for CZTSe-based solar cells using selenization of vacuum deposited metallic precursors (Mo/Cu/Sn/Cu/Zn/Sn/Se) has been shown. Power conversion efficiencies up to 8.0% have been achieved. Particular attention has been paid to show the reproducibility issue in the process, which is degraded by the improvable control of the precursor composition. As an attempt to further increase device efficiencies, different strategies have been tested such as using a tiny amount of Ge, using a Na doped back contact, assessing the effect of the Se capping layer, or treating the absorber surface. The power conversion efficiency of kesterite devices is significantly improved (+1.4% absolute and +50 mV V_{OC}) with a surface treatment consisting in etching in KMnO₄/H₂SO₄ and (NH₄)₂S solutions followed by a post-deposition annealing. In the latter case, a substantial light soaking treatment is required for the device to reveal its maximum power conversion efficiency of 9.4%. All other attempts to substantially improve device performances do not meet the expected success, suggesting that a universal activation step to boost kesterite device efficiencies has not been found by the community yet as suggested in Ref. 24.

SUPPLEMENTARY MATERIAL

See [supplementary material](#) for the impact of the SnSe₂ secondary phase on the PV properties of the kesterite device.

ACKNOWLEDGMENTS

This research was supported by the H2020 Programme under the project STARCELL (H2020-NMBP-03-2016-720907) and the Laboratoire d'excellence LANEF in Grenoble (ANR-10-LABX-51-01).

- ¹I. Repins, N. Vora, C. Beall, S.-H. Wei, Y. Yan, M. Romero, G. Teeter, H. Du, B. To, M. Young, and R. Noufi, *MRS Online Proc.* **1324**, 11 (2011).
- ²W. Wang, M. T. Winkler, O. Gunawan, T. Gokmen, T. K. Todorov, Y. Zhu, and D. B. Mitzi, *Adv. Energy Mater.* **4**, 1301465 (2014).
- ³See http://www.solar-frontier.com/eng/news/2017/1220_press.html for the announcement of the PV record.
- ⁴A. Polizzotti, I. L. Repins, R. Noufi, S.-H. Wei, and D. B. Mitzi, *Energy Environ. Sci.* **6**, 3171–3182 (2013).
- ⁵X. Liu, Y. Feng, H. Cui, F. Liu, X. Hao, G. Conibeer, D. B. Mitzi, and M. Green, *Prog. Photovoltaics Res. Appl.* **24**(6), 879–898 (2016).
- ⁶S. López-Marino, Y. Sánchez, M. Espíndola-Rodríguez, X. Alcobé, H. Xie, M. Neuschitzer, I. Becerril, S. Giraldo, M. Dimitrievska, M. Placidi, L. Fourdrinier, V. Izquierdo-Roca, A. Pérez-Rodríguez, and E. Saucedo, *J. Mater. Chem. A* **4**(5), 1895–1907 (2016).
- ⁷C. Andres, S. G. Haass, Y. E. Romanyuk, and A. N. Tiwari, *Thin Solid Films* **633**, 141–145 (2017).
- ⁸M. Neuschitzer, J. Marquez, S. Giraldo, M. Dimitrievska, M. Placidi, I. Forbes, V. Izquierdo-Roca, A. Pérez-Rodríguez, and E. Saucedo, *J. Phys. Chem. C* **120**(18), 9661–9670 (2016).
- ⁹S. López-Marino, Y. Sánchez, M. Placidi, A. Fairbrother, M. Espíndola-Rodríguez, X. Fontané, V. Izquierdo-Roca, J. Lopez-Garcia, L. Calvo-Barrio, A. Perez-Rodríguez, and E. Saucedo, *Chem. - Eur. J.* **19**(44), 14814–14822 (2013).
- ¹⁰A. Fairbrother, E. Garcia-Hemme, V. Izquierdo-Roca, X. Fontane, F. A. Pulgarin-Agudelo, O. Vigil-Galan, A. Perez-Rodríguez, and E. Saucedo, *J. Am. Chem. Soc.* **134**, 8018 (2012).
- ¹¹L. Grenet, M. A. A. Suzon, F. Emieux, and F. Roux, *ACS Appl. Energy Mater.* **1**(5), 2103 (2018).
- ¹²L. Grenet, S. Bernardi, D. Kohen, C. Lepoittevin, S. Noël, N. Karst, A. Brioude, S. Perraud, and H. Mariette, *Sol. Energy Mater. Sol. Cells* **101**, 11–14 (2012).
- ¹³L. Grenet, P. Grondin, K. Coumert, N. Karst, F. Emieux, F. Roux, R. Fillon, G. Altamura, H. Fournier, P. Faucherand, and S. Perraud, *Thin Solid Films* **564**, 375–378 (2014).
- ¹⁴G. Altamura and J. Vidal, *Chem. Mater.* **28**(11), 3540–3563 (2016).
- ¹⁵G. Larramona, S. Levchenko, S. Bourdais, A. Jacob, C. Choné, B. Delatouche, C. Moisan, J. Just, T. Unold, and G. Dennler, *Adv. Energy Mater.* **5**(24), 1501404 (2015).
- ¹⁶M. C. Johnson, C. Wrasman, X. Zhang, M. Manno, C. Leighton, and E. S. Aydil, *Chem. Mater.* **27**(7), 2507–2514 (2015).
- ¹⁷G. Brammert, M. Buffière, C. Verbist, S. Oueslati, J. Bekaert, H. ElAnzeery, K. B. Messaoud, S. Syhayaraj, M. Batuk, J. Hadermann, C. Köble, M. Meuris, and J. Poortmans, in *Proceedings of the 42nd IEEE PVSC* (2015), pp. 1–4.
- ¹⁸S. Schorr, *Sol. Energy Mater. Sol. Cells* **95**(6), 1482–1488 (2011).
- ¹⁹Y. F. Qi, D. X. Kou, W. H. Zhou, Z. J. Zhou, Q. W. Tian, Y. N. Meng, X. S. Liu, Z. L. Du, and S. X. Wu, *Energy Environ. Sci.* **10**, 2401 (2017).
- ²⁰S. Lie, J. M. R. Tan, W. Li, S. W. Leow, Y. F. Tay, D. M. Bishop, O. Gunawan, and L. H. Wong, *J. Mater. Chem. A* **6**, 1540–1550 (2018).
- ²¹M. Neuschitzer, Y. Sanchez, T. Olar, T. Thersleff, S. Lopez-Marino, F. Oliva, M. Espindola-Rodríguez, H. Xie, M. Placidi, V. Izquierdo-Roca, I. Laueremann, K. Leifer, A. Pérez-Rodríguez, and E. Saucedo, *Chem. Mater.* **27**(15), 5279–5287 (2015).
- ²²L. Grenet, R. Fillon, G. Altamura, H. Fournier, F. Emieux, P. Faucherand, and S. Perraud, *Sol. Energy Mater. Sol. Cells* **126**, 135–142 (2014).
- ²³S. Bourdais, C. Choné, B. Delatouche, A. Jacob, G. Larramona, C. Moisan, A. Lafond, F. Donatini, G. Rey, S. Siebentritt, A. Walsh, and G. Dennler, *Adv. Energy Mater.* **6**(12), 1502276 (2016).
- ²⁴S. K. Wallace, D. B. Mitzi, and A. Walsh, *ACS Energy Lett.* **2**(4), 776–779 (2017).